

Sedimentation equilibrium of colloidal platelets in an aligning magnetic field

Hendrik Reich¹ and Matthias Schmidt^{2,3}

¹*Deutscher Wetterdienst, Frankfurter Straße 135, D-63067 Offenbach, Germany*

²*Theoretische Physik II, Physikalisches Institut, Universität Bayreuth, D-95440 Bayreuth, Germany*

³*H. H. Wills Physics Laboratory, University of Bristol, Royal Fort, Tyndall Avenue, Bristol BS8 1TL, United Kingdom*

(Received 22 January 2010; accepted 11 March 2010; published online 14 April 2010)

We consider colloidal platelets under the influence of gravity and an external aligning (magnetic) field. The system is studied using a fundamental measure density functional theory for model platelets of circular shape and vanishing thickness. In the gravity-free case, the bulk phase diagram exhibits paranematic-nematic phase coexistence that vanishes at an upper critical point upon increasing the strength of the aligning field. Equilibrium sedimentation profiles display a paranematic-nematic interface, which moves to smaller (larger) height upon increasing the strength of gravity (the aligning field). The density near the bottom of the system decreases upon increasing the strength of the aligning field at fixed strength of gravity. Using a simple model for the birefringence properties of equilibrium states, we simulate the color variation with height, as can be observed in samples between crossed polarizers. © 2010 American Institute of Physics.

[doi:10.1063/1.3378264]

I. INTRODUCTION

Dispersions of platelike colloidal particles display a wide range of interesting physical phenomena, including the thermodynamic stability of liquid crystalline phases,^{1–6} formation of tactoids,^{7,8} nematic wetting of substrates,^{9,10} and capillary effects.¹¹ Examples of discotic colloids include gibbsite^{5,6} and montmorillonite^{12–15} particles. Due to the diamagnetic anisotropy of the particles, such dispersions can be susceptible to the influence of a magnetic field and pronounced changes of the orientational distribution of the particles can be induced. As a result not only the location of, e.g., the isotropic-nematic (IN) phase transition, may change,¹⁶ but also effects in the isotropic phase appear, such as field induced birefringence.¹⁷

The case of platelets is less well studied theoretically when compared to thin hard rods where Onsager (second-virial) theory¹⁸ predicts that at low values of the external field the first-order IN phase transition persists, but that this transition vanishes at a critical point above a certain (critical) field strength. In an extension to thick rods,¹⁹ using the Parsons–Lee density functional theory (DFT),^{20–22} the dependence of the critical field strength on the width-to-length ratio of the rods was investigated. Ref. 23 addresses the phase behavior of hard rods in an orienting external field. In Ref. 24, the authors calculate the phase coexistence curves for both rods and platelets for the case of negative anisotropic polarizability on the basis of Onsager theory and find a tricritical point. Quasi-two-dimensional Monte Carlo simulations of a colloidal dispersion composed of magnetic plate-like particles are reported in Ref. 25

Both integral equation theory^{26–28} and DFT^{9,29,30} are powerful tools for the theoretical study of platelet systems. A fundamental measure DFT for circular hard platelets with

vanishing thickness³¹ was shown to give results for the coexistence densities and order parameter at coexistence of the IN transition in bulk that are superior to results from Onsager theory when compared to simulation data (see Ref. 32 for a detailed discussion). The peculiar nature of the bulk IN phase transition of this model lies in its weakness (as measured by the density jump at coexistence) and the low degree of order in the coexisting nematic phase.

The simultaneous presence of both a magnetic field and gravity has been investigated in Ref. 33, where the microstructure of magnetite colloids was studied experimentally, and in Ref. 15, where the preparation and sedimentation behavior of magnetite-covered clay particles was addressed. The effect of gravity alone on liquid crystal phase transitions of colloidal platelets was investigated in Ref. 5 using Monte Carlo simulations.

The current work is motivated by recent experiments using gibbsite platelets,¹⁶ where sedimented samples were exposed to the influence of a magnetic field. The particles possess negative diamagnetic anisotropy $\Delta\chi$ and hence tend to align their normals perpendicular to the magnetic field. The field was directed horizontally and the sample was placed on a rotating stage with vertical axis of rotation. In this setup, the nematic director was found to align with the vertical direction and sedimentation gradients were obtained using polarization microscopy, which is a simple, yet powerful experimental technique for the investigation of liquid crystalline ordering.¹⁷ Such experimental setups consist of a light source that emits a parallel light beam say along the x axis, a polarizer, the sample with the colloidal platelets, a second polarizer (analyzer) that is at 90° to the first polarizer, and a camera that records the thus obtained image. No light can pass the two crossed polarizers when the sample is iso-

tropic. From the spectrum (and hence the color) of the transmitted light, information about the degree of nematic ordering in the sample can be obtained.

We use the theory of Ref. 31 to consider a corresponding simple model platelet system using particles with circular shape and vanishing thickness. These are exposed to the simultaneous influence of gravity and an effective field that aligns the nematic director in the vertical direction. We calculate equilibrium density profiles and nematic order parameter profiles as a function of height and investigate their dependence on the strength of both external fields. Inspired by the experimental setup, we calculate the birefringence color variation with height using a simple model for the birefringent properties of the inhomogeneous dispersion. The resulting color charts can be, in principle, compared to images from polarization microscopy.

This paper is organized as follows. In Sec. II, we define the model interactions. Section III describes the DFT. Results for phase behavior, density, and order parameter profiles are presented in Sec. V. We conclude in Sec. VI.

II. MODEL PLATELETS IN GRAVITATIONAL AND MAGNETIC FIELDS

We consider a system of circular hard platelets of radius R and vanishing thickness. The pair interaction potential $\phi(\mathbf{r}, \mathbf{u}, \mathbf{u}')$ between two particles with orientations \mathbf{u} and \mathbf{u}' (normal to the platelet face) and center-center separation vector \mathbf{r} is infinite if the two particles overlap and vanishes otherwise. An external potential acts on the system, that models the influence of an aligning field, gravity, and two confining walls,

$$V_{\text{ext}}(\mathbf{r}, \mathbf{u}) = V_0 \sin^2 \theta + k_B T \frac{z}{\xi_g} + V_w(z, \theta), \quad (1)$$

where z is the vertical coordinate, θ is the angle between the platelet orientation \mathbf{u} and the z axis, V_0 determines the strength of the aligning field, k_B is the Boltzmann constant, T is absolute temperature, ξ_g is the gravitational height, and $V_w(z, \theta)$ models the presence of the top and the bottom wall. The gravitational height is

$$\xi_g = \frac{k_B T}{mg}, \quad (2)$$

where g is the gravitational acceleration and m is the particle buoyancy mass. The two parallel walls are impenetrable to the particle shapes and are modeled by

$$V_w(z, \theta) = \begin{cases} 0, & R \sin \theta < z < L - R \sin \theta, \\ \infty, & \text{otherwise,} \end{cases} \quad (3)$$

where L is the distance between the walls; we restrict ourselves to $L=100R$ in the following.

The strength of the aligning field, as measured by V_0 , can be related to the strength of the magnetic field that acts on the dispersion and the value of the diamagnetic anisotropy of the particles, see Appendix A for the derivation. For the case where the diamagnetic anisotropy $\Delta\chi > 0$, such that the platelets tend to align their normals parallel to the field in order to minimize the magnetic energy, the strength of the

aligning field is $V_0 = B^2 \Delta\chi / 2$, where B is the strength of the magnetic field. For the case of diamagnetic anisotropy $\Delta\chi < 0$, one can argue that a magnetic field that rotates sufficiently fast around the z axis gives rise to an effective alignment effect that can be modeled by Eq. (1), albeit with a reduced strength of $V_0 = -B^2 \Delta\chi / 4$, see Appendix A.³⁴ Considering typical values for temperature $T=300$ K, diamagnetic anisotropy $\Delta\chi = -10^{-22} \text{ J/T}^2$, and magnetic field $B=4T$, one finds the relevant range of interaction parameters $0 \leq V_0 / k_B T \leq 0.1$, to which we will restrict ourselves in the following. We expect platelet-platelet interactions due to induced magnetic dipoles to be small (see Appendix B) and will ignore such energetic contributions.

III. DFT FOR HARD PLATELETS

The grand potential in an ensemble of chemical potential μ , temperature T , and system volume V , as a functional of the one-body density distribution $\rho(\mathbf{r}, \mathbf{u})$, where \mathbf{r} is the position vector and the unit vector \mathbf{u} indicates the particle orientation is expressed as

$$\begin{aligned} \tilde{\Omega}([\rho], T, V, \mu) = & \int d\mathbf{r} d\mathbf{u} \rho(\mathbf{r}, \mathbf{u}) [\ln(\rho(\mathbf{r}, \mathbf{u}) \Lambda^3) - 1] + F_{\text{exc}}[\rho] \\ & + \int d\mathbf{r} d\mathbf{u} \rho(\mathbf{r}, \mathbf{u}) [V_{\text{ext}}(\mathbf{r}, \mathbf{u}) - \mu], \end{aligned} \quad (4)$$

where the first term on the right hand side is the Helmholtz free energy functional of an ideal gas of uniaxial rotators, the excess free energy functional $F_{\text{exc}}[\rho]$ describes the influence of interparticle interactions, and the third term on the right hand side of Eq. (4) is the external contribution to the grand potential; $F_{\text{exc}}[\rho]$ depends parametrically on T and V (which is suppressed in the notation). For the equilibrium density $\rho(\mathbf{r}, \mathbf{u})$ the variational principle²⁹ states that

$$\frac{\delta \tilde{\Omega}([\rho], T, V, \mu)}{\delta \rho(\mathbf{r}, \mathbf{u})} = 0. \quad (5)$$

Inserting the solution of Eq. (5) into Eq. (4) yields the true value of the grand potential in equilibrium. Using this framework for actual applications requires to have an approximation for $F_{\text{exc}}[\rho]$. Here we use the fundamental measure theory (FMT) proposed in Ref. 31, see, e.g., Equations (7)–(15) in Ref. 32 for the detailed definition of $F_{\text{exc}}[\rho]$ for a one-component system of platelets.

We first consider the case of the bulk system under the influence of the aligning field alone, i.e., $\xi_g \rightarrow \infty$ and $V_w = 0$. The density is spatially constant and, due to uniaxial symmetry of the nematic phase, depends only on the angle θ between the particle orientation and the nematic director, $\rho(\mathbf{r}, \mathbf{u}) = \rho(\theta)$. In the isotropic phase $\rho(\mathbf{r}, \mathbf{u}) = \rho = \text{const}$. Hence we take into account only the aligning field in the external potential [first term in Eq. (1)] and calculate, via Eqs. (4) and (5), the equation of state $\rho(\mu)$ and the variation of the nematic order parameter, $S(\rho)$, in the nematic phase; the nematic order parameter is defined as

$$S = \int d\theta \sin(\theta) \psi(\theta) [3 \cos^2(\theta) - 1]/2, \quad (6)$$

where the orientational distribution function is $\psi(\theta) = \rho(\theta)/\rho$, with the bulk density obtained by integration over the unit sphere, $\rho = \int d\mathbf{u} \rho(\theta)$. Phase coexistence is calculated by equating the chemical potential and the grand potential (and hence the pressure) in the two coexisting phases; equality of temperature is trivially satisfied in hard core systems.

The above theory for bulk can be used as the basis for a treatment of the system under the influence of gravity within the local-density approximation (LDA). On length scales that are large as compared to the particle size, the influence of gravity can be modeled by a spatially varying chemical potential $\tilde{\mu}(z)$, which depends linearly on height, $\tilde{\mu}(z) = \mu - k_B T z / \xi_g$. The constant μ is then a free parameter that we choose to ensure that the total number of particles $N = \text{const}$ for different values of the strength of the aligning fields, V_0 . The number of particles N per lateral system area A (perpendicular to the z direction) is obtained from the density profiles via

$$\frac{N}{A} = \int_0^L dz \rho(z). \quad (7)$$

The height-dependent density profile $\rho(z)$ and order parameter profile $S(z)$ are then obtained from the bulk equation of state via $\rho(z) = \rho(\tilde{\mu}(z))$ and $S(z) = S(\tilde{\mu}(z))$. The LDA treatment is valid in the limit $L/\xi_g = \text{const}$ and $R/L \rightarrow 0$.

In order to investigate the effects caused by finite (scaled) system height R/L , and hence the influence of interparticle correlations on the density distribution, we use the fully nonlocal fundamental-measure theory of Ref. 31 and solve the minimization condition (5) for $\rho(z, \theta)$. Again μ is adjusted in order to keep $N/A = \text{const}$ upon variation of the strength of the external influence via V_0 and ξ_g . The total density at height z (irrespective of orientation) is then $\rho(z) = \int d\theta \sin(\theta) \rho(z, \theta)$. The nematic order parameter profile $S(z)$ is obtained from the full density field by setting $\psi(\theta)$ to $\psi(z, \theta) = \rho(z, \theta) / \rho(z)$ in the definition (6). We restrict ourselves to $L = 100R$ in the following. Confinement in more narrowly spaced slits (without further fields) was investigated in Ref. 35. The results for density profiles $\rho(z)$ and order parameter profiles $S(z)$ can be utilized to compute the color variation with height of samples between crossed polarizers, as is laid out in the following.

IV. SIMULATION OF BIREFRINGENCE COLORS OF NEMATIC SAMPLES

The birefringent properties of dispersions of anisotropic colloidal particles originate from the difference in refractive indices parallel and vertical to the optical axis \mathbf{u} of the particles.³⁶ In the situation that we consider, the optical axis is parallel to the z axis since the platelets tend to align with their normal parallel to this axis. The propagation direction of the light is assumed to be along the x axis.

The angle between the polarization direction of the light beam (after it has passed the polarizer) and the z axis is $\pi/4$. When crossing the sample, the light beam is split into two

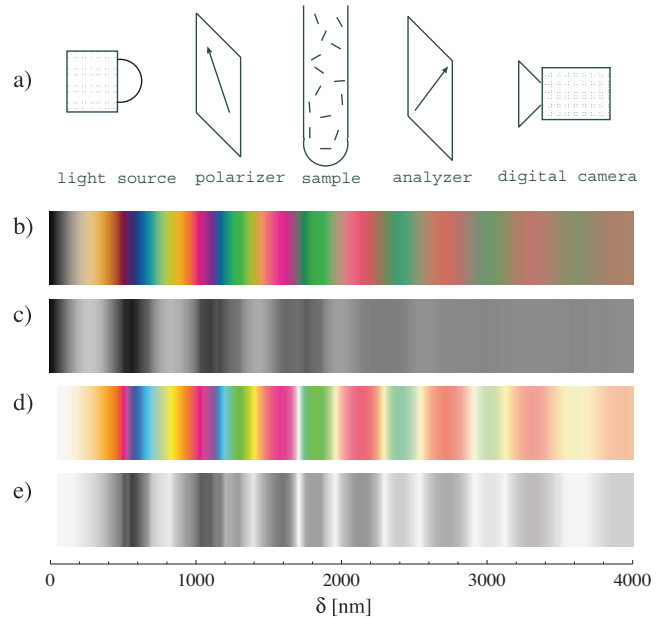


FIG. 1. (a) Illustration of the experimental setup, consisting of a white light source, polarizer, colloidal sample, analyzer, and digital camera aligned with the x axis. The arrows indicate the direction of the polarizers. The z direction is vertical. (b) Color variation with retardation δ in range 0–4000nm; (c) the corresponding intensity variation; (d) the result of the chromoscope procedure; and (e) the corresponding intensity variation.

parts, one polarized perpendicular and one polarized parallel to the z -axis. Because both parts of the light beam make an angle of $\pi/4$ and $-\pi/4$, respectively, with the analyzer, only a fraction of the initial intensity of the light beam reaches the camera, see Fig. 1(a) for a schematic illustration. The different refractive indices along these directions imply differing speed of light, which generates a retardation δ . The intensity of the transmitted light that reaches the camera depends on the wavelength λ of the light and is given by

$$I(\lambda, \delta) = I_0(\lambda) \sin^2(\pi \delta / \lambda), \quad (8)$$

where we model the intensity of the incident light $I_0(\lambda)$ as black body radiation with Planck distribution

$$I_0(\lambda) = \frac{2hc^2}{\lambda^5} \left[\exp\left(\frac{hc}{\lambda k_B T_i}\right) - 1 \right]^{-1}, \quad (9)$$

where h is the Planck's constant, c is the speed of light, and T_i is the temperature of the black body. We assume that the retardation δ is related to the properties of the sample at height z by

$$\delta = a \rho(z) S(z) R^3, \quad (10)$$

where the parameter a (with dimension of length) depends linearly on the thickness of the sample and on the difference between the refractive indices in the two perpendicular directions.^{16,17} We disregard such sample- and material-specific dependence in the following and will treat a as an adjustable parameter.

The full spectrum $I(\lambda)$ (suppressing the dependence on δ in the notation) is then projected onto a three-dimensional color space in two steps. First, the so-called XYZ tristimulus values are calculated via

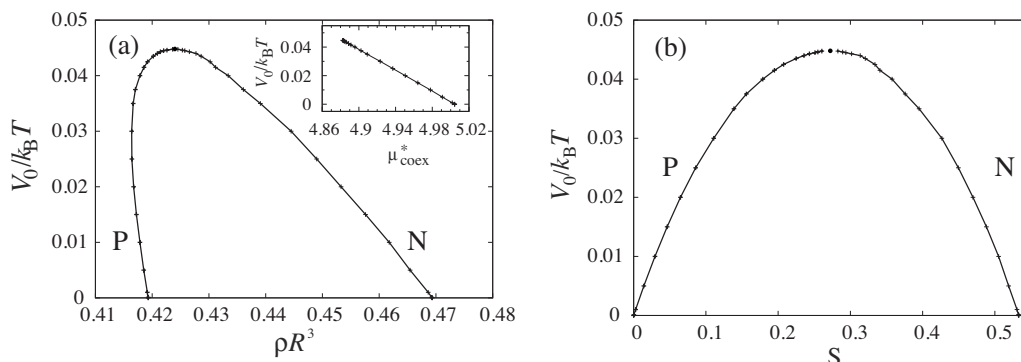


FIG. 2. (a) Variation of the paranematic (P) and nematic (N) coexistence densities (horizontal axis) with the strength of the external aligning field $V_0/k_B T$ (vertical axis). The critical point is located at $\rho R^3=0.423$ and $V_0/k_B T=0.045$ (filled circle). The inset shows the variation of the chemical potential at PN coexistence, μ_{coex}^* , with the field parameter $V_0/k_B T$ (vertical axis). (b) Same as (a), but as a function of the order parameter S in the paranematic and nematic phase (horizontal axis). Lines are guides to the eye.

$$X = \int I(\lambda) \bar{x}(\lambda) d\lambda, \quad Y = \int I(\lambda) \bar{y}(\lambda) d\lambda, \quad Z = \int I(\lambda) \bar{z}(\lambda) d\lambda, \quad (11)$$

where $\bar{x}(\lambda)$, $\bar{y}(\lambda)$, and $\bar{z}(\lambda)$ are the standardized CIE color-matching functions³⁷ for red, green, and blue, respectively, as determined by physiological experiments. Note that X , Y , and Z depend on retardation δ . Then the set of XYZ values is converted to the RGB color space by multiplication with the appropriate 3×3 conversion matrix A , hence $(R, G, B) = (X, Y, Z) \cdot A$. Negative values of one of the components of the RGB vector, which can potentially occur because of the fact that the RGB color space is smaller than the XYZ color space, are set to zero and hence cut off. Gamma correction is applied in order to model the situation of bright illumination, i.e., such that the intensity inside of dark regions is enhanced relative to regions of high intensity. Gamma correction amounts to the mapping $R \rightarrow R^{1/1.9}$, $G \rightarrow G^{1/1.9}$, and $B \rightarrow B^{1/1.9}$. The resulting color chart, plotted as a function of retardation δ for $T_i=6000$ K, a value that is appropriate for modeling white light, is shown in Fig. 1(b). Note that the total intensity that is transmitted varies with retardation δ . In order to illustrate this effect, we show in Fig. 1(c) the corresponding intensity, obtained via one of the standard conversion procedures to obtain grayscale values as the weighted average $0.3R+0.59G+0.11B$.

It is interesting to compare the color chart obtained by the procedure above with an alternative one where the brightness is adjusted in order to maximize the intensity for each value of retardation *separately*. A useful procedure that performs this task is Berry's chromascope,³⁸ defined by the mapping $R \rightarrow R/M$, $G \rightarrow G/M$, $B \rightarrow B/M$, where the normalization is $M = \max(R, G, B)$. This implies that at least one of the three resulting color channel is at maximum intensity of unity, see Fig. 1(d) for the result as a function of δ . It is very striking how different the resulting sequence of colors is to that shown in Fig. 1(b). Again the brightness is not uniform, as can be seen in Fig. 1(e), where we plot the corresponding intensity $0.3R+0.59G+0.11B$, using the RGB values obtained by the cromascope procedure.³⁹

The choice of color chart depends on the experimental situation that is modeled. In the present case, we are inter-

ested in the case where the incident light is the same for all height values, hence we will use the bare color chart, Fig. 1(b), in order to visualize the theoretical height-dependent profiles. We will use results for $\rho(z)$ and $S(z)$ together with Eqs. (8) and (10) as an input to Eq. (11), in order to illustrate the theoretical profiles. Clearly all effects due to scattering and adsorption from the sample are omitted in this treatment.

V. RESULTS

A. Influence of a magnetic field on the IN bulk phase transition

The result for the phase diagram of hard platelets under the influence of an aligning magnetic field are shown in Fig. 2(a) as a function of the coexistence densities (horizontal axis) and the scaled field strength $V_0/k_B T$ (vertical axis). In the field-free case, $V_0=0$, the theory gives reasonable agreement with values for the transition densities as obtained from computer simulations.^{40,41} Upon increasing $V_0/k_B T$ the paranematic and nematic coexistence densities initially shift to lower densities. The density difference decreases slightly with increasing values of the scaled field strength $V_0/k_B T$. Above $V_0/k_B T=0.02$, the paranematic coexistence density starts to *increase* again, while the nematic coexistence density continues to decrease. Both branches of the binodal merge at a critical point at $\rho_c R^3=0.423$ and $V_{0,c}/k_B T=0.045$; for $V_0 > V_{0,c}$ the phase transition ceases to exist. The variation of the chemical potential at paranematic-nematic coexistence, μ_{coex}^* , is plotted in the inset of Fig. 2(a); we use a scaled chemical potential $\mu^* = \mu/(k_B T)$. We find that μ_{coex}^* decreases monotonically and almost linearly with increasing $V_0/k_B T$. The variation of the order parameter S at coexistence is shown in Fig. 2(b) as a function of $V_0/k_B T$. As might be expected, the field has an aligning effect and leads to non-vanishing nematic order, $S > 0$ in the paranematic phase. For small values of $V_0/k_B T$ the coexistence value of S in the paranematic phase increases monotonically with increasing field strength; the value of S in the nematic phase at coexistence decreases accordingly. The latter behavior is consistent with the shift of the coexistence density to lower densities [Fig. 2(a)]; this is associated with a lower order parameter in

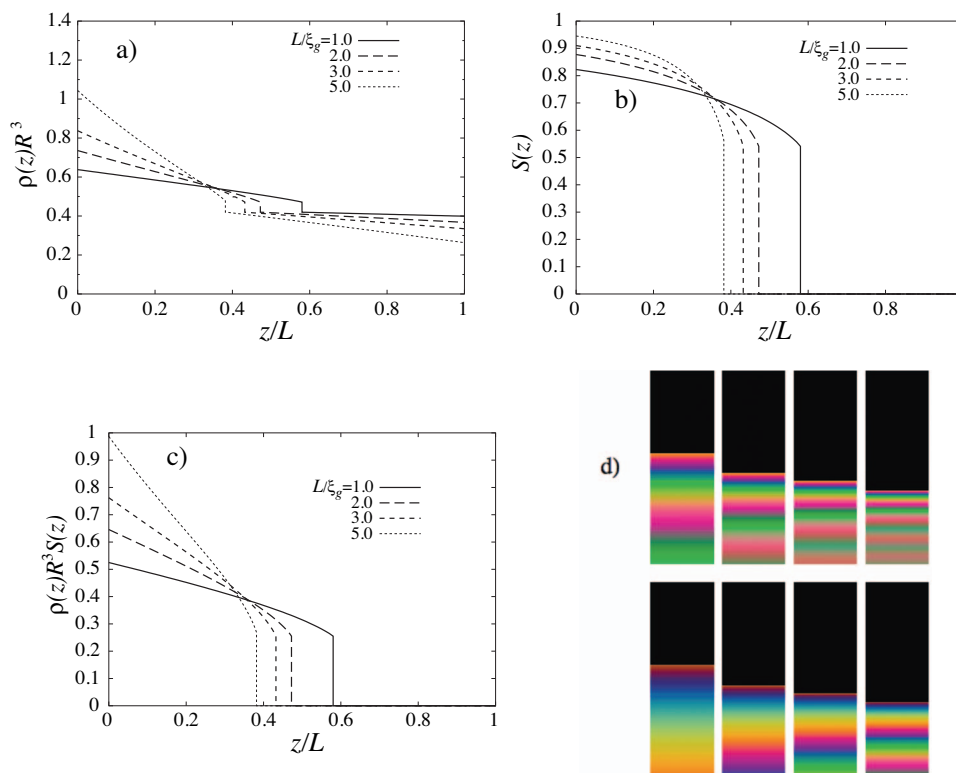


FIG. 3. (a) Density profile $\rho(z)R^3$ as a function of the scaled height z/L , where L is the system height, as obtained from LDA for different ratios of the system size and the gravitational length $L/\xi_g=1, 2, 3$, and 5 (as indicated). Walls are located at $z=0$ and $z=L$. (b) Order parameter profile $S(z)$ and (c) product $\rho(z)R^3S(z)$ for the same parameters as in (a). (d) Simulated variation of the birefringence colors with height, as observable in sedimented samples between crossed polarizers, for $a=3600$ nm (first row) and 1800 nm (second row) for the same values of L/ξ_g (increasing from left to right).

the field-free case. This effect overcompensates the ordering effect caused by the external field.

B. Sedimentation equilibrium in the field-free case

We next consider the influence of gravity alone on the system. The mean density, which is kept constant in the following, is chosen as $N/(AL)=0.5/R^3$. In Fig. 3(a), density profiles $\rho(z)$ from LDA are shown as a function of the scaled height, z/L , for a sequence of values of the ratio of system height and gravitational length, $L/\xi_g=1, 2, 3$, and 5 . Upon increasing the value of L/ξ_g , the density near the bottom of the system increases while the density in the upper region of the system decreases; hence, the particles accumulate at the bottom of the sample. Due to the constraint $N/A=\text{const}$ both effects are intimately coupled. The interface between the lower (nematic) and upper (isotropic) phase appears as a sharp kink because the LDA does not resolve nonlocal correlations. In Fig. 3(b), results for the local order parameter $S(z)$ are shown as a function of the scaled height z/L . In agreement with the observed increase of the density, we find an increase of $S(z)$ in the lower part of the system upon increasing L/ξ_g . The product of order parameter and density, $\rho(z)R^3S(z)$, as shown in Fig. 3(c) displays an almost linear decrease upon increasing height in the nematic phase. Using this quantity, in Fig. 3(d), we display the sequence of birefringence colors that would occur under crossed polarizers. Results for two different values of a , modeling, e.g., different sample thicknesses, are shown in Fig. 3(d) for $a=3600$ nm (first row) and 1800 nm (second row) with temperature T_i

$=6000$ K of the incident white light. The compression of the nematic phase upon increasing strength of gravity is apparent from (i) the movement of the position of the IN interface toward smaller heights and (ii) the fact that the birefringence orders appear in more rapid succession (hence in narrower bands) upon increasing the value of L/ξ_g .

We next consider the effects of finite system size, $L=100R$, and show results from FMT as a function of the scaled height z/R for different values of the inverse gravitational height $R/\xi_g=0.01, 0.02$, and 0.03 again for constant overall (area) density, $N/A=\text{const}$. The density [Fig. 4(a)] and order parameter [Fig. 4(b)] profiles and the product of both [Fig. 4(c)] indicate smooth variation of the density across the IN interface. The fact that $S(z)$ decreases to (small) plateau values, rather than to zero, in the upper region is entirely due to numerical reasons. Interesting structuring is apparent at both walls, where $S(z)$ reaches values close to unity, indicative of parallel alignment of the particles with the (hard) walls. For comparison, we also show the density and order parameter profile for the free IN interface, which is the appropriate limit encountered for $R/\xi_g \rightarrow 0$. The present mean-field-like treatment does not include effects due to thermal capillary wave fluctuations.⁴² The calculated birefringence color variation with height is shown in Fig. 4(d). Comparing to the case of LDA [Fig. 3(d)] this clearly illustrates the diffuse nature of the IN interface, as well as the orientational order that appears close to the upper wall. Note, however, that a translation to experiment is much less straightforward than in the case of LDA, due to the strong

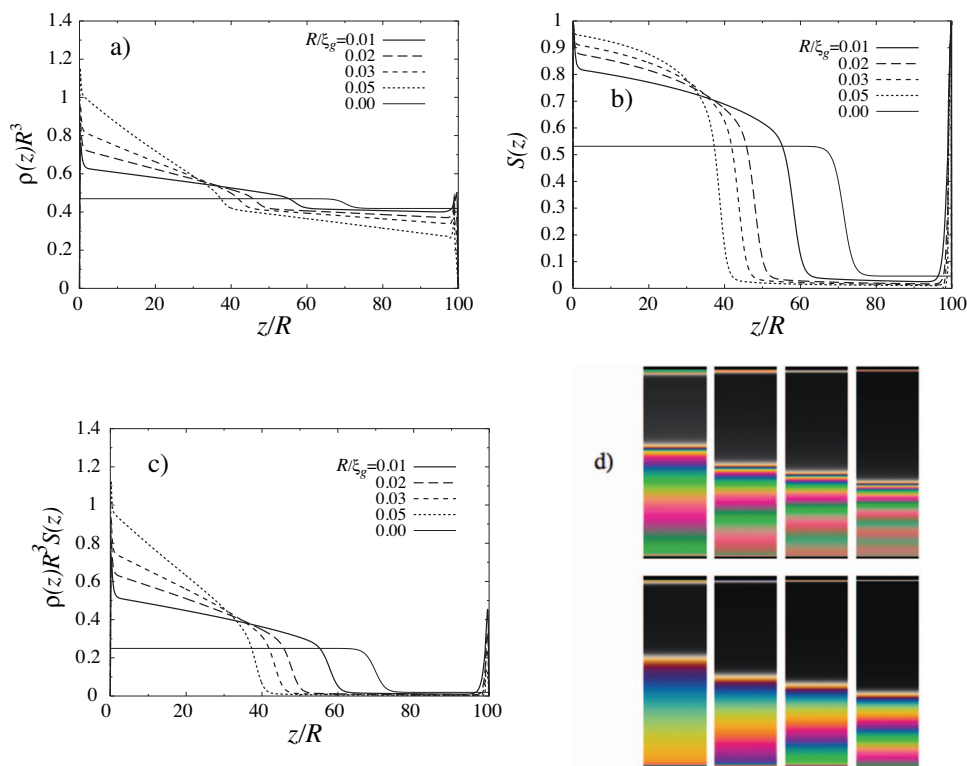


FIG. 4. (a) Density profile $\rho(z)R^3$ as a function of the scaled height z/R , where R is the particle radius, as obtained from non-local FMT for different values of the inverse gravitational length $R/\xi_g=0.01, 0.02, 0.03, 0.05$, and 0.10 (as indicated). The density profile of the free IN interface in the field-free case $R/\xi_g=0$ (thick solid line) is also shown; the Gibbs dividing surface is located at $z/R=70$. Walls are located at $z=0$ and $z=L$ with the system length $L=100R$. (b) Order parameter profile $S(z)$ and (c) product $\rho(z)R^3S(z)$ for the same parameters as in (a). (d) Simulated birefringence for $a=3600$ nm (first row) and 1800 nm (second row) for the same values of R/ξ_g (increasing from left to right).

confinement of the system, $L=100R$, and hence small overall system size. Light propagation on such small scales will be governed by further effects that are neglected in our treatment. Nevertheless we find this graphical representation to be a useful means to illustrate our theoretical results.

C. Sedimentation equilibrium of hard platelets in a magnetic field

We next consider the system under the simultaneous influence of both gravity and an aligning field that orients the particles preferentially along the vertical axis. We first discuss results obtained from LDA. In Fig. 5(a), density profiles $\rho(z)$ are shown as a function of the scaled height z/ξ_g for the case of $L/\xi_g=1$, i.e., such that the system height equals the gravitational length. We again keep $N/A=\text{const}$ (by choosing the value of the chemical potential appropriately) and consider a range of values of the scaled strength of the aligning field, $V_0/k_B T=0, 0.005, 0.02$, and 0.1 . Upon increasing the field strength, the position of the interface moves upwards in the system, consistent with the expectation that the nematic phase would grow with increasing the field strength. For values of $V_0/k_B T$ larger than the critical value, rather than a steplike interface a continuous decrease of density upon increasing height z is found. Quite unexpectedly, the density at the bottom of the system *decreases* upon increasing the value of $V_0/k_B T$. We attribute this to originate from ordering effects in the paranematic phase and subsequently increasing density in the upper part of the system. Due to the constant total number of particles, the density then decreases at the

bottom of the system. The variation of the order parameter, shown in Fig. 5(b), as a function of height, confirms this scenario. The nematic order in the paranematic phase increases with increasing field strength. The value of the order parameter near the bottom of the system remains almost constant upon increasing the field strength. This might be explained with the decreasing density found at the bottom [see Fig. 5(a)] and hence decreasing nematic order. The product $\rho(z)R^3S(z)$, as shown in Fig. 5(c), indicates a decrease at the bottom of the system for increasing field strength, as can be expected from the individual behavior of $\rho(z)$ and $S(z)$. The strongest effects on the birefringence colors [Fig. 5(d)] occur in the upper part of the sample, which even turns bright for the largest value of the aligning field considered.

We display results from the nonlocal FMT in Fig. 6. Here we use z/R as a scaled height coordinate. The gravitational strength is controlled by R/ξ_g , which we set to $R/\xi_g=0.01$. Again, two hard walls are located at $z/R=0$ and at $z/R=100$. The chemical potential μ^* is chosen to ensure $N/A=\text{const}$ for all values of $V_0/k_B T$ considered. As above we display scaled density profiles $\rho(z)R^3$ [Fig. 6(a)], order parameter profiles $S(z)$ [Fig. 6(b)] the product $\rho(z)R^3S(z)$ [Fig. 6(c)], and birefringence color variation with height [Fig. 6(d)].

Comparing the results from LDA and FMT, one observes remarkable differences. Within the z -dependent FMT, we find ordering effects at both hard walls as well as density oscillations at the upper wall, see Fig. 6(a). In contrast to this, the LDA profiles are monotonic, consistent with the fact

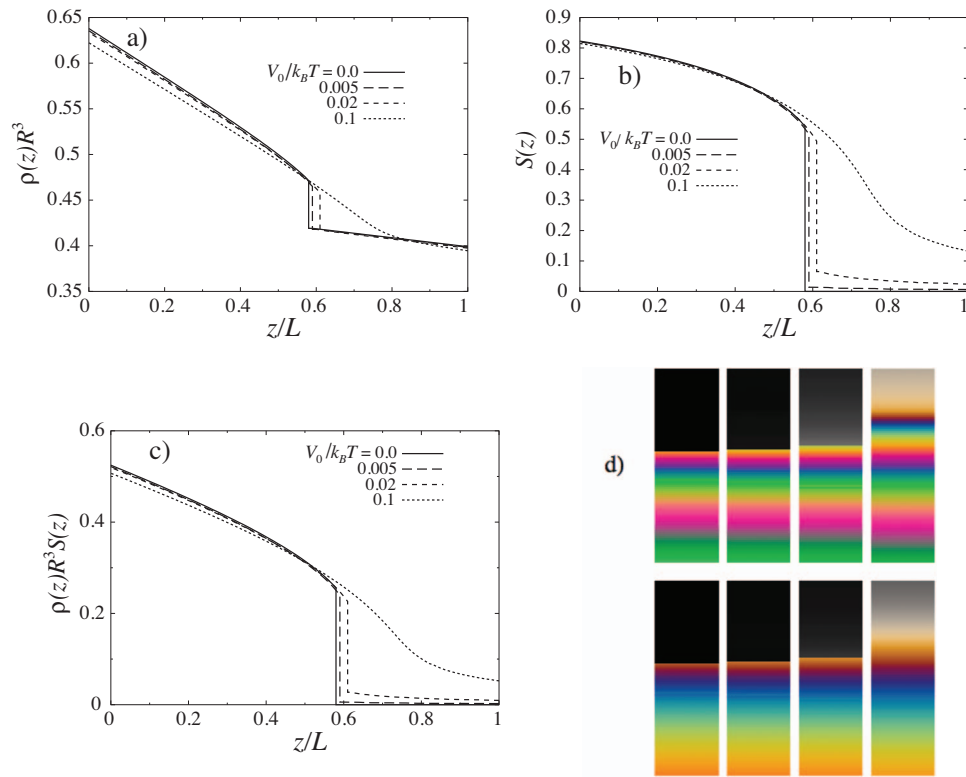


FIG. 5. (a) Density profiles $\rho(z)R^3$ as a function of the scaled system height z/L , where L is the system height, for different values of the field parameter $V_0/k_B T=0, 0.005, 0.02$, and 0.1 as obtained from LDA. The chemical potential μ^* is chosen to ensure that the number of particles per area is constant, $N/A=\text{const}$, for all values of $V_0/k_B T$. (b) Same as (a), but for the order parameter profile $S(z)$. (c) Same as (a), but for the product of order parameter and density profiles, $\rho(z)R^3S(z)$. (d) Simulated birefringence for $a=3600$ nm (first row) and 1800 nm (second row) for the same values of $V_0/k_B T$.

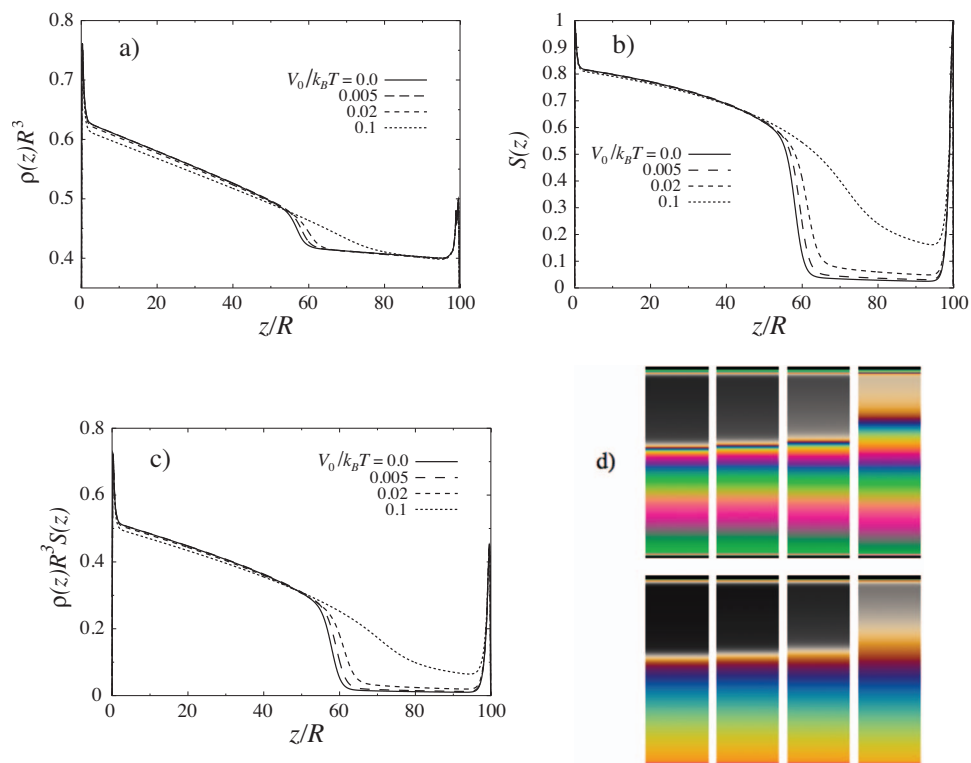


FIG. 6. (a) Density profile $\rho(z)$ as a function of the scaled height z/R , where R is the particle radius obtained from FMT for different values of the field parameter $V_0/k_B T=0, 0.005, 0.02, 0.1, 0.5$, and 1.0 (as indicated). Hard walls are located at $z=0$ and $z=L$ with the total system height $L=100R$. The inverse gravitational length is fixed to $R/\xi_g=0.01$. (b) Same as (a), but for the order parameter profile $S(z)$. (c) Same as (a), but for the product of order parameter and density profile $\rho(z)R^3S(z)$. (d) Simulated birefringence for $a=3600$ nm (first row) and 1800 nm (second row) for the same values of $V_0/k_B T$.

that the LDA is a local theory which treats different heights z of the system as independent from each other. Also the nematic-paranematic interface shows much more gradual variation with z in FMT. Nevertheless the LDA describes the unexpected properties such as the decrease of density at the bottom with increasing field strength correctly.

VI. CONCLUSIONS

In summary, we have investigated the properties of a model dispersion of monodisperse platelets under gravity and inside of a magnetic field. Due to their nonvanishing diamagnetic anisotropy, $\Delta\chi \neq 0$, the platelets tend to align their normals with the vertical direction. We argued that this can be achieved either with a magnetic field that is pointing in the vertical direction and particles that possess $\Delta\chi > 0$ or, using a rotating setup, a horizontal field and particles with $\Delta\chi < 0$ (as realized in recent experiments^{16,17}).

We have used both a nonlocal FMT version of DFT as well as an LDA treatment. LDA captures the basic features of the inhomogeneous density and order parameter profiles correctly (such as accumulation of particles in the bottom region), but fails to reproduce the adsorption at the hard walls and effects due to finite width of the interface between nematic and paranematic phases. The FMT describes such nonlocal effects and, based on earlier comparison to simulations,¹⁰ we expect the density profiles to be semiquantitatively, if not quantitatively, accurate. It would be highly desirable to carry out corresponding computer simulations for the present model. An interesting topic for such studies could be to calculate the paranematic-nematic phase diagram in the presence of an aligning field. In particular obtaining the precise location of the critical point would be a very worthwhile issue. Recall that the nematic phase at coexistence (in the field-free case) possesses an unusually small nematic order parameter, $S \sim 0.5$. Here we find the critical field strength, beyond which there is no phase coexistence, to be also very small, $V_{0,c}/k_B T = 0.045$. As this is obtained from a mean-field treatment, the true value might differ and it would be interesting to see how much so. The location of the critical point is reflected in the shape of the sedimentation gradients, i.e., whether or not those exhibit a clear paranematic-nematic interface or, corresponding to paths in the bulk phase diagram above the critical point, smooth variation with height.

The LDA results form an appropriate description of the macroscopic density gradients, and results can be compared, in principle, to experimental findings from setups such as those of Refs. 16 and 17. The FMT results describe more strongly confined systems, i.e., particles with radii $R = 500$ nm inside of capillaries with spacing $L = 50$ μm . Using a simple theory for the birefringence properties, we have calculated the macroscopic color variation for sedimented samples between crossed polarizers. We have shown in detail that a corresponding color chart consisting of triplets of RGB color values for each value of retardation δ can be calculated in a simple way.

ACKNOWLEDGMENTS

We thank Henk Lekkerkerker, David van der Beek, Sir Michael Berry, Susanne Klein, Chris Newton, Jonathan Phillips, and Gemma Weston for useful discussions. This work is supported by the EPSRC (Grant No. EP/E065619) and the Liquid Crystals Group of HP Laboratories, Bristol. Financial support by the DFG within the SFB840/A3 is gratefully acknowledged.

APPENDIX A: ADIABATIC ALIGNMENT OF PLATELETS IN A ROTATING MAGNETIC FIELD

The orientation-dependent part of the external potential [first term on the right hand side of Eq. (1)] can be derived from an external magnetic field that acts on the dispersion. We take the platelets to be diamagnetic and characterized by a diamagnetic susceptibility tensor per particle, which is diagonal in the platelet frame of reference, $\hat{\chi} = \text{diag}(\chi_{\parallel}, \chi_{\parallel}, \chi_{\perp})$, where the first two components indicate the directions in the platelet plane, and the third component indicates the platelet normal. In general the diamagnetic anisotropy $\Delta\chi \equiv \chi_{\parallel} - \chi_{\perp}$ will be nonzero. Inclining the platelet by an angle θ with respect to the z axis, such that $\mathbf{u} = (0, \sin \theta, \cos \theta)$, we can use the rotation matrix $\hat{\mathbf{D}} = ((1, 0, 0), (0, \cos \theta, \sin \theta), (0, -\sin \theta, \cos \theta))$ to express the susceptibility tensor of the tilted platelet as $\hat{\chi}' \equiv \hat{\mathbf{D}}^{-1} \cdot \hat{\chi} \cdot \hat{\mathbf{D}} = ((\chi_{\parallel}, 0, 0), (0, c^2 \chi_{\parallel} + s^2 \chi_{\perp}, sc \Delta\chi), (0, sc \Delta\chi, s^2 \chi_{\parallel} + c^2 \chi_{\perp}))$, where $s = \sin \theta$ and $c = \cos \theta$.

We first consider the case $\Delta\chi > 0$, where the platelets tend to align their normals parallel to the field. We choose the field in the vertical direction, $\mathbf{B} = (0, 0, B)$, and obtain the magnetic energy per particle as $V_{\text{magn}}(\theta) = \frac{1}{2} \mathbf{B} \cdot \hat{\chi}' \cdot \mathbf{B}^t = \frac{1}{2} B^2 \chi_{\perp} + \frac{1}{2} B^2 \Delta\chi \sin^2 \theta$, where the superscript t indicates transposition. The first term forms an irrelevant constant, and from comparing the second term with Eq. (1), we obtain $V_0 = B^2 \Delta\chi / 2$.

For $\Delta\chi < 0$, the platelet normals align perpendicular to the direction of the field. This leaves the angle of rotation of the platelet orientation around the direction of the field undetermined. This rotational symmetry can be broken by considering a rotating magnetic field that lies in the xy plane and rotates around the z axis, $\mathbf{B} = (B \cos \phi, B \sin \phi, 0)$, where $\phi = \omega t$, with ω being the angular frequency of rotation and t being time. The magnetic energy is $V_{\text{magn}}(\theta, \phi) = \frac{1}{2} \mathbf{B}^t \cdot \hat{\chi}' \cdot \mathbf{B} = \frac{1}{2} B^2 (\chi_{\parallel} - \Delta\chi \sin^2 \theta \cos^2 \phi)$. Assuming that the rotation of the field is much faster than the motion of the platelet, such that the position of the particle can be considered as static during the rotation, we average over one cycle, $\bar{V}_{\text{magn}}(\theta) = \frac{1}{2\pi} \int_0^{2\pi} d\phi V_{\text{magn}}(\theta, \phi) = \frac{1}{2} \chi_{\parallel} B^2 - \frac{1}{4} B^2 \Delta\chi \sin^2 \theta$. The first term again contributes an irrelevant constant to the total potential energy. Comparing the second term to the first term in Eq. (1) yields $V_0 = -B^2 \Delta\chi / 4$. Note that $V_0 > 0$, because $\Delta\chi < 0$, hence again a uniaxial situation is encountered. However the effective strength of the aligning potential is only half of that in the case of $\Delta\chi > 0$, because of the averaging over “favorable” and “unfavorable” alignment of platelet and field during each rotation cycle.

APPENDIX B: ESTIMATE OF THE STRENGTH OF DIPOLAR PAIR INTERACTION

For the case of parallel dipoles that are oriented perpendicular to their relative distance vector, the energy of two interacting magnetic dipoles is $E = \mu_0 m^2 / r^3$, where $m = \chi B / 2$ is the magnetic moment, r is the spatial separation between the two dipoles and $\mu_0 = 4\pi \cdot 10^{-7} \text{ N/A}^2$. Assuming the diamagnetic susceptibility of the material per volume to possess a value of the order of $\chi_V = -10^{-5}$ yields the diamagnetic susceptibility per particle $\chi = \chi_V V / \mu_0 = 10^{-21} \text{ J/T}^2$, where $V = \pi D R^2 \approx 10^6 \text{ nm}^3$ is the volume of a platelet with thickness, say, $D = 20 \text{ nm}$ and radius $R = 100 \text{ nm}$. This yields $E = 10^{-27} \text{ J} = 2.4 \cdot 10^{-7} k_B T$ for $T = 300 \text{ K}$, and having chosen a typical particle separation distance $r = 200 \text{ nm}$. Comparing this with the magnitude of the strength of interaction with the external field, $V_0 = 0.1 k_B T$, shows that the latter constitutes the dominant effect.

- ¹F. M. van der Kooij, K. Kassapidou, and H. N. W. Lekkerkerker, *Nature (London)* **406**, 868 (2000).
- ²F. M. van der Kooij, D. van der Beek, and H. N. W. Lekkerkerker, *J. Phys. Chem. B* **105**, 1696 (2001).
- ³S. D. Zhang, P. A. Reynolds, and J. S. van Duijneveldt, *J. Chem. Phys.* **117**, 9947 (2002).
- ⁴S. D. Zhang, P. A. Reynolds, and J. S. van Duijneveldt, *Mol. Phys.* **100**, 3041 (2002).
- ⁵D. van der Beek, T. Schilling, and H. N. W. Lekkerkerker, *J. Chem. Phys.* **121**, 5423 (2004).
- ⁶D. van der Beek, A. V. Petukhov, S. M. Oversteegen, G. J. Vroege, and H. N. W. Lekkerkerker, *Eur. Phys. J. E* **16**, 253 (2005).
- ⁷A. A. Verhoeff, R. H. J. Otten, P. van der Schoot, and H. N. W. Lekkerkerker, *J. Phys. Chem. B* **113**, 3704 (2009).
- ⁸R. H. J. Otten and P. van der Schoot, *Langmuir* **25**, 2427 (2009).
- ⁹M. Bier, L. Harnau, and S. Dietrich, *J. Chem. Phys.* **125**, 184704 (2006).
- ¹⁰D. van der Beek, H. Reich, P. van der Schoot, M. Dijkstra, T. Schilling, R. Vink, M. Schmidt, R. van Roij, and H. N. W. Lekkerkerker, *Phys. Rev. Lett.* **97**, 087801 (2006).
- ¹¹M. M. Piniero, A. Galindo, and A. O. Parry, *Soft Matter* **3**, 768 (2007).
- ¹²J. Connolly, J. S. van Duijneveldt, S. Klein, C. Pizzey, and R. M. Richardson, *Langmuir* **22**, 6531 (2006).
- ¹³J. Connolly, J. S. van Duijneveldt, S. Klein, C. Pizzey, and R. M. Richardson, *J. Phys.: Condens. Matter* **19**, 156103 (2007).
- ¹⁴J. S. van Duijneveldt, S. Klein, E. Leach, C. Pizzey, and R. M. Richardson,

- J. Phys.: Condens. Matter* **17**, 2255 (2005).
- ¹⁵C. Galindo-González, J. de Vicente, M. M. Ramos-Tejada, M. T. Lopez-Lopez, F. Gonzalez-Caballero, and J. D. G. Duran, *Langmuir* **21**, 4410 (2005).
- ¹⁶D. van der Beek, P. Davidson, H. H. Wensink, G. J. Vroege, and H. N. W. Lekkerkerker, *Phys. Rev. E* **77**, 031708 (2008).
- ¹⁷D. van der Beek, A. V. Petukhov, P. Davidson, J. Ferre, J. P. Jamet, H. H. Wensink, G. J. Vroege, W. Bras, and H. N. W. Lekkerkerker, *Phys. Rev. E* **73**, 041402 (2006).
- ¹⁸A. R. Khokhlov and A. N. Semenov, *Macromolecules* **15**, 1272 (1982).
- ¹⁹S. Varga, G. Jackson, and I. Szalai, *Mol. Phys.* **93**, 377 (1998).
- ²⁰J. D. Parsons, *Phys. Rev. A* **19**, 1225 (1979).
- ²¹S. D. Lee, *J. Chem. Phys.* **87**, 4972 (1987).
- ²²S. D. Lee, *J. Chem. Phys.* **89**, 7036 (1988).
- ²³H. Graf and H. Löwen, *J. Phys.: Condens. Matter* **11**, 1435 (1999).
- ²⁴S. Varga, G. Kronome, and I. Szalai, *Mol. Phys.* **98**, 693 (2000).
- ²⁵A. Satoh and Y. Sakuda, *Mol. Phys.* **107**, 1621 (2009).
- ²⁶D. L. Cheung, L. Anton, M. P. Allen, and A. J. Masters, *Phys. Rev. E* **73**, 061204 (2006).
- ²⁷D. L. Cheung, L. Anton, M. P. Allen, and A. J. Masters, *Phys. Rev. E* **76**, 041201 (2007).
- ²⁸D. L. Cheung, L. Anton, M. P. Allen, and A. J. Masters, *Phys. Rev. E* **77**, 011202 (2008).
- ²⁹R. Evans, *Adv. Phys.* **28**, 143 (1979).
- ³⁰M. Bier, L. Harnau, and S. Dietrich, *Phys. Rev. E* **69**, 021506 (2004).
- ³¹A. Esztermann, H. Reich, and M. Schmidt, *Phys. Rev. E* **73**, 011409 (2006).
- ³²H. Reich, M. Dijkstra, R. van Roij, and M. Schmidt, *J. Phys. Chem. B* **111**, 7825 (2007).
- ³³V. M. Buzmakov, *Colloid J.* **57**, 11 (1995).
- ³⁴This was independently obtained by H. N. W. Lekkerkerker (private communication).
- ³⁵H. Reich and M. Schmidt, *J. Phys.: Condens. Matter* **19**, 326103 (2007).
- ³⁶The optical axis is the direction in which the refractive index does not depend on the polarization direction of the incident light.
- ³⁷*Kaye and Laby Tables of Physical and Chemical Constants*, 16th ed. (UK National Physical Laboratory, Teddington, 1995). See online edition at www.kayelab.npl.co.uk.
- ³⁸M. V. Berry, *New J. Phys.* **4**, 74 (2002).
- ³⁹It is interesting to note that the “bare” interference colours of Fig. 1(b) resemble the Michel–Levy chart of D. Flinn and G. Newall (University of Liverpool), whereas the cromascope version, Fig. 1(d), is more akin to the Interference color chart for common minerals (after Kerr); see, e.g., F. D. Bloss, *An Introduction to the Methods of Optical Crystallography* (Holt, Rinehart, and Winston, New York, 1961).
- ⁴⁰D. Frenkel and R. Eppenga, *Phys. Rev. Lett.* **49**, 1089 (1982).
- ⁴¹R. Eppenga and D. Frenkel, *Mol. Phys.* **52**, 1303 (1984).
- ⁴²N. Akino, F. Schmid, and M. P. Allen, *Phys. Rev. E* **63**, 041706 (2001).